



Synthesis and characterization of PVA embedded with peanut-shaped Ag_cAu_s nanoparticles: optical and electrical properties

Ravi Kumar¹ · Rajiv Kumar^{2,3} · Pawan K. Sharma² · Annu Sharma¹

Received: 4 October 2021 / Revised: 28 June 2022 / Accepted: 15 July 2022 /

Published online: 29 July 2022

© The Author(s), under exclusive licence to Springer-Verlag GmbH Germany, part of Springer Nature 2022

Abstract

Peanut-shaped Ag core Au shell (Ag_cAu_s) nanoparticles (NPs) synthesized by facile chemical reduction approach have been used to alter the optical and electrical parameters of polyvinyl alcohol (PVA). Synthesized Ag_cAu_s NPs and Ag_cAu_s PVA nanocomposites (NC) have been examined using high-resolution transmission electron microscopy (HRTEM), field emission scanning electron microscopy (FE-SEM), X-ray diffraction (XRD) and UV–Visible absorption spectroscopy. HRTEM and FE-SEM confirmed the presence of peanut-shaped NPs with Au shell over Ag core. Williamson-Hall method has been used to compute crystallite size and induced lattice strain. Linear as well as nonlinear optical parameters have been computed using absorption data. Decline in the optical band gap (E_g) from 4.7 to 2.57 eV and increase in the Urbach's energy (E_u) from 0.91 to 2.12 eV of PVA on addition of 0.36 wt% of Ag_cAu_s NPs are significant outcomes of this study. In addition, significant increase in refractive index, optical conductivity and nonlinear optical parameters of PVA with increasing concentration of Ag_cAu_s NPs has been observed. The current–voltage characteristics have been examined to verify the conduction mechanisms responsible for increased conductivity of Ag_cAu_s PVA NC.

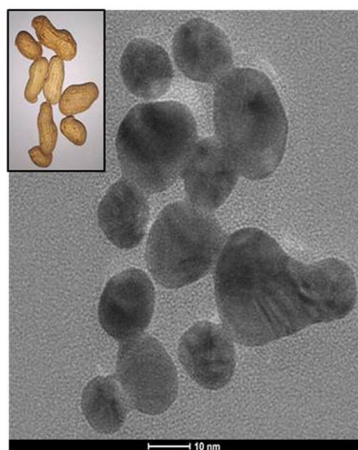
✉ Annu Sharma
asharma@kuk.ac.in

¹ Department of Physics, Kurukshetra University, Kurukshetra, Haryana 136119, India

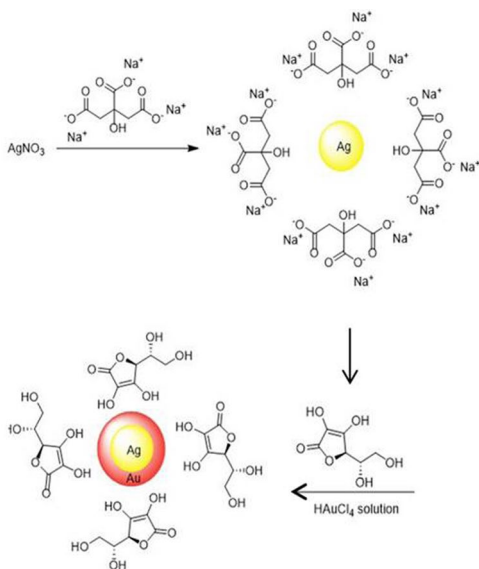
² Department of Chemistry, Kurukshetra University, Kurukshetra, Haryana 136119, India

³ Ch. Mani Ram Godara Government College for Women, Bhodia Khera, Fatehabad 125050, India

Graphical abstract



Peanut shape Ag_cAu_s NPs



Keywords Core–shell · Polyvinyl alcohol · Optical properties · Optical band gap · Urbach's energy

Introduction

Monometallic nanoparticles (NPs) of noble metals such as Ag and Au are being increasingly investigated as they exhibit tuneable surface plasmon resonance peak (SPR) on varying their size, shape and the surrounding matrix, resulting in their unique optical properties [1–3] making them potential contenders for design of high-speed nonlinear devices, such as ultrafast optical switches and optical limiters [4]. Among the noble metals, NPs of Ag exhibit higher plasmonic efficiency and superior electromagnetic enhancement in the visible range. This makes Ag NPs materials of choice for exploring potential in optoelectronics, photovoltaics, and sensing application [5, 6]. Despite interesting properties displayed by Ag NPs, their toxicity and easy oxidation are major deterrents that hinder their widespread usage [7, 8]. An effective way to address these challenges is, to encapsulate Ag NPs in an outer shell of another noble metal such as Au which will not only increase their functionality but also their stability as Au NPs have inherent attributes such as biocompatibility, resistance to oxidation, easy preparation, and homogeneity [9–11]. Moreover, it is an ideal way of augmenting beneficial properties of both Ag as well as Au NPs [9]. Such core–shell NPs (CSNPs) are frequently sought-after in comparison with monometallic NPs for realization of hybrid materials as they display enhanced linear and nonlinear optical properties, catalytic and electronic properties that can be modified by altering the diameter

of core (Ag) and thickness of outer shell (Au). As a result, Ag core Au shell (Ag_cAu_s) NPs have broad range of potential applications in diverse domains such as biosensors [12], optical [9], biomedical [13], antibacterial [14], electronics [15], surface-enhanced Raman scattering (SERS) [10, 16], and sensors [17].

Moreover, the novel attributes exhibited by such CSNPs can be modified by controlling their shape. Lai et al. [18] synthesized hexagonal nanorings of Ag core Au shell NPs using hexagonal nanoplates of Ag and studied structure-dependent optical characteristics. Khlebtsov et al. [19] prepared Au core Ag shell cuboids and dumbbells with the help of seed-mediated anisotropic growth process and analysed their structural and optical properties. Rai et al. [20] fabricated triangular Au core Ag shell NPs and characterized them by transmission electron microscopy (TEM), X-ray photoelectron spectroscopy (XPS), UV–Visible spectroscopy and atomic force microscopy (AFM). Yin et al. [21] fabricated Ag core Au shell dendrites by hydrothermal corrosion method and studied their application in SERS. Li et al. [22] prepared shuttle-like Au core Ag shell nanostructures and studied their electrocatalytic activity. Senedrin et al. [23] fabricated Ag core and Au shell nanoprisms by using silver prisms as seeds and reducing Au on their surfaces. Encapsulation of CSNPs into a suitable matrix protects them from agglomeration as well as imparts new and improved attributes to host matrix. Polyvinyl alcohol (PVA), a water soluble polymer is a strong contender to be used as host material due to its well-known attributes such as high transmission, easy processability and biocompatibility [24, 25]. Moreover, it provides long-time stability to CSNPs [26, 27]. Comprehensive studies on optical and electrical properties of PVA by embedding Ag_cAu_s NPs have seldom been reported. However, some reports are available on tuning of optical properties of PVA by embedding Ag/Au NPs. Bulla et al. [28] prepared biosynthesized Ag-PVA nanocomposites (NC) films and studied their optical and structural properties. They ascertained that E_g of PVA decreased with addition of Ag NPs. Shamy et al. [29] fabricated PVA-Ag NC films and analysed their optical and mechanical properties utilizing UV–Visible spectroscopy, TEM, X-ray diffractometer and mechanical test machine (AMETEK). Mahmoud et al. [30] synthesized PVA-Ag NC films and analysed their optical and antimicrobial properties. These NC films were characterized by using TEM, UV–Visible spectroscopy, and Fourier-transform infrared spectroscopy (FTIR). They observed that PVA NC films showed good antibacterial activity against *Escherichia coli*, *Staphylococcus aureus* and *Bacillus subtilis*.

In the present study, peanut-shaped Ag_cAu_s NPs have been synthesized, characterized and further used to fabricate Ag_cAu_s PVA NC. Structural, optical (linear and nonlinear) and electrical properties of resulting Ag_cAu_s PVA NCs have been investigated.

Experimental

Materials

Chloroauric acid ($\text{HAuCl}_4 \cdot x\text{H}_2\text{O}$) (Mol. wt. 339.78 g/mol) was purchased from Molychem, Mumbai. Polyvinyl alcohol (Mol. wt. 1,25,000 g/mol) was purchased

from CDH, and silver nitrate (AgNO_3) (Mol. wt. 169.87 g/mol), trisodium citrate dihydrate ($\text{Na}_3\text{C}_6\text{H}_5\text{O}_7 \cdot 2\text{H}_2\text{O}$) (Mol. wt. 294.10 g/mol), and L-Ascorbic acid ($\text{C}_6\text{H}_8\text{O}_6$) (Mol. wt. 176.13 g/mol) were acquired from Rankem, India.

Experimental procedure

For fabrication of Ag_cAu_s NPs, 2 mL of 17.66 mM AgNO_3 and 2 mL of 40.80 mM trisodium citrate aqueous solution were poured into 35 mL of double deionized water kept in a two-necked round-bottom flask, under continuous stirring and refluxing for 30 min. Appearance of dark yellow colour suggested the growth of Ag NPs. Subsequently, the colloidal solution of Ag NPs was cooled rapidly. In the next step, 1 mL of 33.49 mM HAuCl_4 and 1 mL of 82.32 mM ascorbic acid aqueous solution were added dropwise into colloidal solution of Ag NPs under constant stirring until its colour changed to wine red, demonstrating the formation of Ag_cAu_s NPs.

To grow films, 1 g PVA was dissolved in double deionized water (25 mL) at a temperature of 30 °C and casted into the Petri dishes. Subsequently, 0.09 wt%, 0.18 wt%, 0.27 wt% and 0.36 wt% colloidal solution of Ag_cAu_s NPs were added to PVA solution under vigorous stirring. The homogeneous solution was poured into Petri dishes, dried and processed under dark conditions at a temperature of 30 °C. Ag_cAu_s PVA NC was obtained after the evaporation of the solvent. A schematic of steps involved is shown in Figs. 1 and 2.

Characterization of Ag_cAu_s PVA NC

TEM by “Tecnai” (operating voltage = 200 kV) was used for revealing the morphological structure and size distribution, of Ag_cAu_s NPs and Ag_cAu_s PVA NC. “Carl Zeiss Ultra Plus” field emission scanning electron microscopy (FE-SEM) along with energy dispersive analysis of X-ray (EDAX) operating voltage 20 kV was used for determining the surface morphology and composition of Ag_cAu_s PVA NC. Bruker D-8 Advance diffractometer ($\text{CuK}\alpha$, $\lambda=0.154$ nm) scanned from 10° to 80° was used for X-Ray diffraction (XRD) studies. Absorption spectra were recorded using Shimadzu UV-3600 Plus UV–VIS–NIR spectrophotometer in the range of 200 nm to 2000 nm. Current–Voltage (I – V) characteristics were studied by two-probe Keithley 6517-B digital electrometer.

Results and discussion

TEM analysis

Figure 3 shows representative TEM images of Ag_cAu_s NPs and Ag_cAu_s PVA NC. Figure 3a demonstrates that Ag_cAu_s NPs have grown longitudinally and have peanut shape (inset of Fig. 3a) with central dark part (core) and relatively lighter external part (shell) thus confirming the formation of Ag_cAu_s NPs. Selected area electron diffraction (SAED) pattern (Fig. 3b) of the sample displays distinct ring patterns which

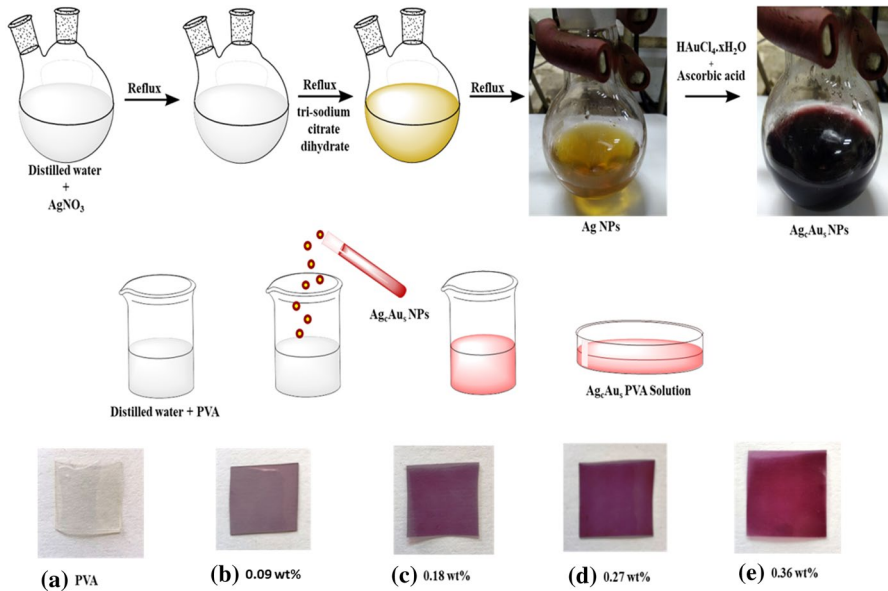


Fig. 1 Illustration of experimental procedure and **i** PVA, **ii–v** Ag_cAu_5 PVA NC films doped with varying amount of Ag_cAu_5 NPs

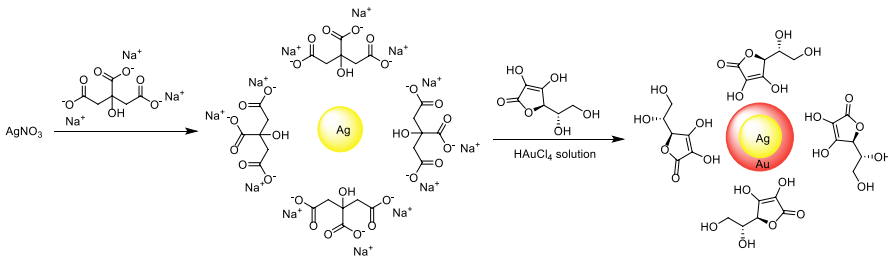


Fig. 2 Schematic mechanism of formation of Ag_cAu_5 NPs

demonstrate their crystalline nature. Further, diffraction spots agree well with (111), (200), (220) and (311) lattice planes of both Ag as well as Au possessing face-centred cubic (fcc) structure. In the case of Ag_cAu_5 NPs, when Au is gradually deposited on Ag, epitaxial growth of Au on Ag do not show any interface because both elements have same chemical nature, interplanar spacing and atomic radii [31]. As a result, SAED pattern of Ag_cAu_5 NPs is indistinguishable. Interestingly, high-resolution transmission electron microscopy (HRTEM) image (Fig. 3c) shows Ag_cAu_5 NPs with peanut shape (peanut shown in inset of Fig. 3c). In addition, magnified view of Fig. 3c as shown in Fig. 3d and e reveals that lattice spacing of Ag (core) is 0.231 and 0.225 nm which matches with the (111) planes of Ag while lattice spacing of Au (shell) is 0.222 and 0.227 nm which matches well with the (111) planes of Au. Moreover, these lattice

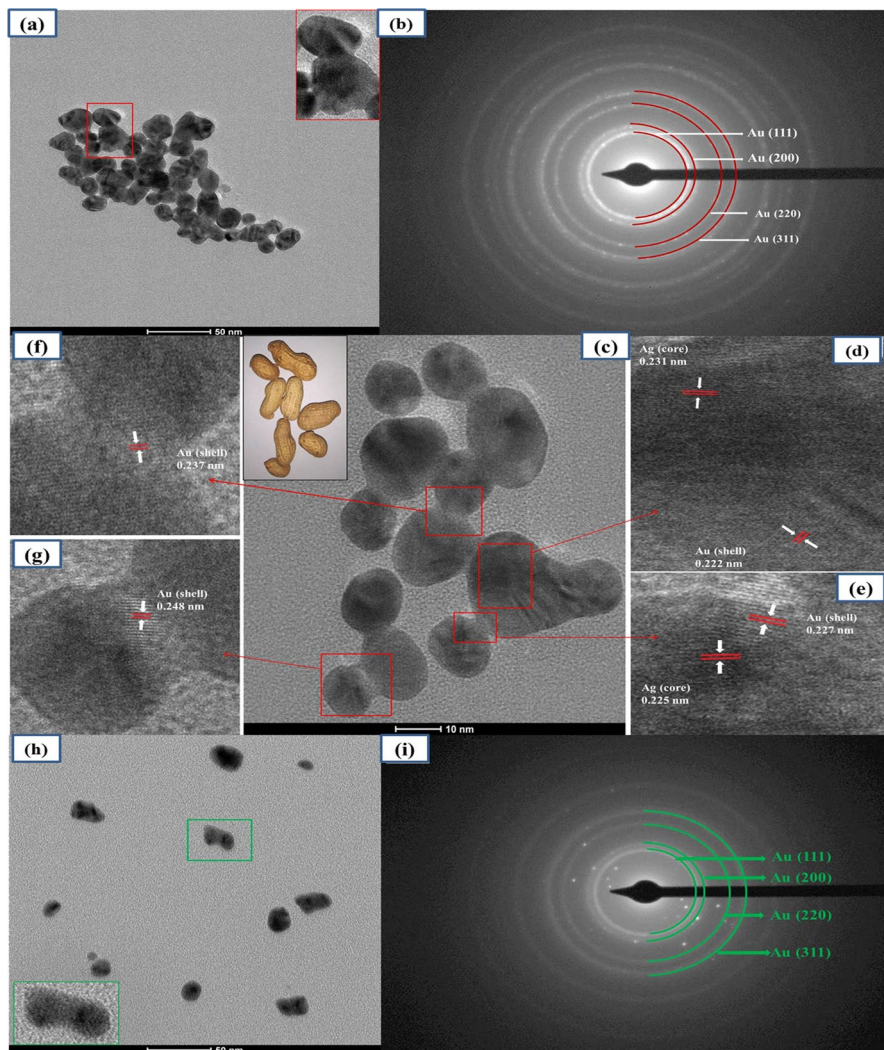


Fig. 3 TEM micrograph of **a** Ag_cAu_s NPs, **b** SAED pattern of Ag_cAu_s NPs, **c** HRTEM image of Ag_cAu_s NPs, **d–g** closer view of HRTEM image of Ag_cAu_s NPs, **h** TEM image of Ag_cAu_s PVA NC, and **i** SAED pattern of Ag_cAu_s PVA NC containing 0.36 wt% of Ag_cAu_s NPs

fringes are in different orientation which provides strong evidence, supporting the formation of Ag_cAu_s NPs. Figure 3f and h shows middle part of peanut-shaped Ag_cAu_s NPs with lattice spacing 0.237 and 0.248 nm which matches with the (111) planes of Au. Furthermore, Fig. 3h and i displays the TEM micrograph of Ag_cAu_s PVA NC and corresponding SAED pattern containing 0.36 wt% of Ag_cAu_s NPs. TEM micrograph of the Ag_cAu_s PVA NC shows scattered peanut-shaped CSNPs present in PVA as shown in Fig. 3h. SAED pattern of Ag_cAu_s PVA NC (Fig. 3i) demonstrates their crystalline

nature and diffraction spots corresponding to the (111), (200), (220) and (311) lattice planes are observed which are similar to lattice planes of Ag and Au with fcc structure.

FESEM analysis

Figure 4a depicts the FESEM image of Ag_cAu_s PVA NC. Figure 4a clearly indicates that most of the Ag_cAu_s NPs have peanut shape morphology with core–shell structure. Thus, both FESEM and TEM images portray that CSNPs have peanut shape. Figure 4b represents the constituent elements present in Ag_cAu_s PVA NC as recorded by EDAX spectrometer. Peaks appearing at 1.6, 2.2, and 3.0 keV energy, in the EDAX spectrum confirm the presence of Au and Ag in Ag_cAu_s PVA NC. It further suggests that content of Ag and Au is 0.11 wt% and 0.09 wt%, respectively.

X-ray diffraction

Figure 5 displays the well-defined XRD results of PVA and Ag_cAu_s PVA NC embedded with 0.36 wt% of Ag_cAu_s NPs. XRD results of pure PVA exhibit signature peak of PVA at 2θ positions of 19.2° and 40.4°, while XRD results of Ag_cAu_s PVA NC reveals distinct peaks indexed at 2θ=38.3° corresponding to (111) lattice plane with interplanar spacing (*d*) 0.244 nm, at 2θ=44.4° corresponding to (200) lattice plane with *d*=0.201 nm, at 2θ=64.5° corresponding to (220) lattice plane with *d*=0.144 nm and at 2θ=77.3° corresponding to (311) lattice plane with *d*=0.123 nm. These lattice planes are similar to standard values of Au with fcc phase and matches with the SAED analysis also. Usually in the case of CSNPs, XRD pattern display peaks originating due to shell metal as core (metal) exist in kinematic diffraction state [32].

The interplanar spacing (*d*) has been evaluated utilizing the formula [33]:

$$2d \sin \theta = n\lambda \tag{1}$$

where λ represents the wavelength of X-rays, order of diffraction and diffraction angle are represented by *n* and θ, respectively.

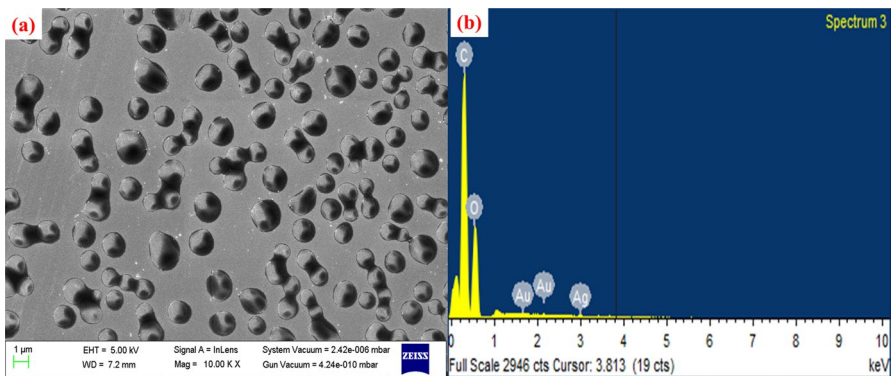
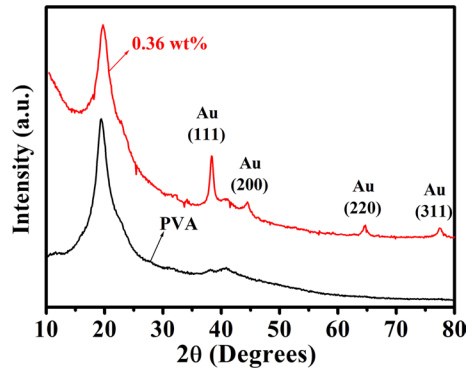


Fig. 4 a FESEM image and b EDAX of Ag_cAu_s PVA NC having 0.36 wt% of Ag_cAu_s NPs

Fig. 5 XRD pattern of PVA and Ag_cAu_s PVA NC



According to Williamsons–Hall (W–H) method, crystallites size (β_D) and lattice strain (β_ϵ) are responsible for broadening (β_T) of the peak observed in XRD pattern [34–36].

$$\beta_T = \beta_D + \beta_\epsilon \quad (2)$$

According to Debye–Scherrer equation:

$$\beta_D = \frac{0.9\lambda}{D \cos \theta} \quad (3)$$

Similarly, XRD peak broadening due to lattice strain can be expressed as:

$$\beta_E = 4\epsilon \tan \theta \quad (4)$$

Thus,

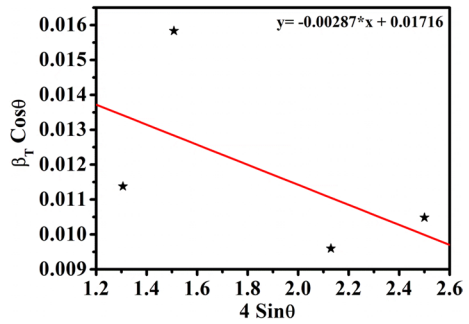
$$\beta_T \cos \theta = \frac{0.9\lambda}{D} + 4\epsilon \sin \theta \quad (5)$$

This equation is a normal straight line equation and is termed as the uniform deformation model (UDM) equation. Figure 6 displays the variation of $\beta_T \cos \theta$ with $4 \sin \theta$ for Ag_cAu_s PVA NC containing 0.36 wt% of Ag_cAu_s NPs. Y-intercept of the best fit line in the data gives crystallite size and slope gives the strain ϵ . The average crystallite size in Ag_cAu_s PVA NC comes out to be 8.06 nm and negative slope shows compressive strain in Ag_cAu_s PVA NC. Gamler et al. [37] also observed compressive strain in CSNPs and suggested that shell thickness and lattice mismatch between core and shell are responsible for this behaviour.

Optical studies

Optical spectroscopy is an ideal tool to ascertain the formation of noble metal NPs (Cu, Ag, and Au) as they show SPR in visible region. Characteristic SPR peak of Cu NPs appears at 590 nm, whereas SPR peak of Ag and Au NPs appear around 420 and 520 nm, respectively. Figure 7 portrays the absorption spectra of colloidal

Fig. 6 Plot of $\beta_T \cos \theta$ versus $4 \sin \theta$ for Ag_cAu_s PVA NC embedded with 0.36 wt% of Ag_cAu_s NPs



Ag NPs and Ag_cAu_s NPs. The presence of SPR peak at 430 nm confirms the formation of Ag NPs, while the presence of peak at 531 nm, endorses the formation of Au shell around Ag NPs. Usually, in the absorption spectra of alloys or binary metal NPs, two different SPR peaks are detected, while in the case of CSNPs, peak arising due to shell metal is observed as core metal is completely encapsulated in shell metal, as a result, absorption spectrum is dominated by shell metal. Murugavelu et al. [38] also observed a peak at 540 nm in the optical spectra of Ag_cAu_s NPs. They ascribed peak at 540 nm to SPR of Au NPs, while peak originating due to Ag NPs was not observed.

Optical spectra of PVA and Ag_cAu_s PVA NCs having varying concentration of Ag_cAu_s NPs is shown in Fig. 8. Figure 8 shows absorption peak of PVA in the UV region, which is close to wavelength of 275 nm. The absorption spectrum for 0.09 wt% Ag_cAu_s PVA NC shows SPR peak centred at 531 nm and its intensity strengthens with increasing content up to 0.36 wt% Ag_cAu_s PVA NC. Additionally, it appears at same wavelength in absorption spectrum of Ag_cAu_s PVA NC and Ag_cAu_s NPs.

Optical spectroscopy data have further used to determine optical energy gap (E_g) and Urbach’s energy (E_u) which are essential input parameters for determining their probable applications in optoelectronic devices. E_g of PVA and Ag_cAu_s PVA NC have been evaluated using Tauc’s power law which relates absorption coefficient (α) with photon energy $h\nu$ [39]:

Fig. 7 Absorption spectra of colloidal NPs

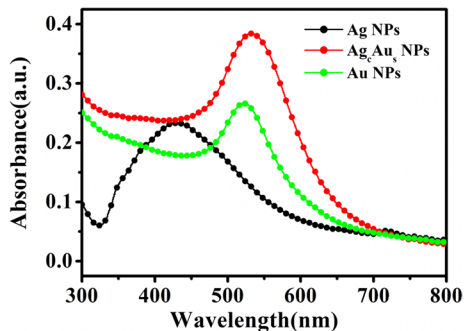
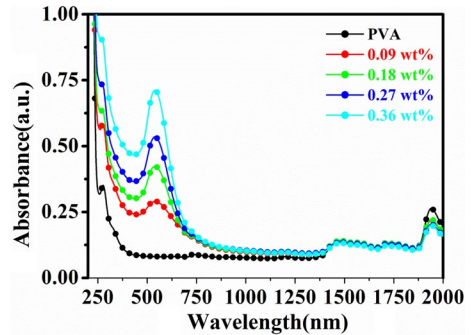


Fig. 8 Optical spectra of PVA and Ag_cAu_s PVA NC



$$\alpha h\nu = C(h\nu - E_g)^a \quad (6)$$

where C is a constant and ‘ a ’ can be 3/2, 1/2, 3 and 2 depending on the nature of the transitions: forbidden direct = 3/2, allowed direct = 1/2, forbidden indirect = 3 and allowed indirect = 2. The absorption coefficient (α) has been obtained by following relation [40]:

$$\alpha d = 2.303 \times A \quad (7)$$

where A and d represent the absorbance and thickness of the film, respectively.

Figure 9a illustrates the variation of $(\alpha h\nu)^{1/2}$ with $h\nu$ for the PVA and Ag_cAu_s PVA NC. Linear fit lines extrapolated to intersect the $h\nu$ axis such that $\alpha = 0$ gives E_g . Figure 9a shows that E_g of PVA (4.7 eV) decreases to 2.57 eV for PVA embedded with 0.36 wt% of Ag_cAu_s NPs and the results are presented in Table 1. Bulla et al. [28] reported that E_g decreased from 3.85 eV for PVA to 3.62 eV for NC with 2 wt% of Ag NPs in PVA matrix. Similarly, Shamy et al. [29] highlighted that E_g decreased from 5.31 eV for PVA to 4.56 eV for NC with 1.5 wt% of Ag NPs in PVA. These results depict that decrease in E_g of PVA by Ag_cAu_s NPs is more in comparison with monometallic NPs.

New localized electronic states formed, due to insertion of Ag_cAu_s NPs produce disorder in the highest occupied molecular orbital (HOMO) and lowest unoccupied molecular orbital (LUMO) gap of PVA and this disorder is measured in terms of E_u . Thus, E_u gives the degree of spread of these newly created impurity states in HOMO–LUMO gap of PVA. E_u has been calculated by using Urbach’s empirical formula [40]:

$$\alpha = \alpha_0 \exp \frac{h\nu}{E_u} \quad (8)$$

where α_0 is a constant.

Reciprocal of the slope of best fit line drawn between $\ln(\alpha)$ and $h\nu$ gives the value of E_u as shown in Fig. 9b. E_u of PVA (0.91 eV) increased to 2.12 eV for 0.36 wt% of Ag_cAu_s NPs in PVA NC films. These results are presented in Table 1.

Hence, when Ag_cAu_s NPs are embedded in PVA, defects in the form of trapping and recombination centres are produced within the HOMO–LUMO region of the

Fig. 9 Plot of **a** $(\alpha hv)^{1/2}$ versus hv **b** $\ln(\alpha)$ versus hv of PVA and Ag_cAu_s PVA NC

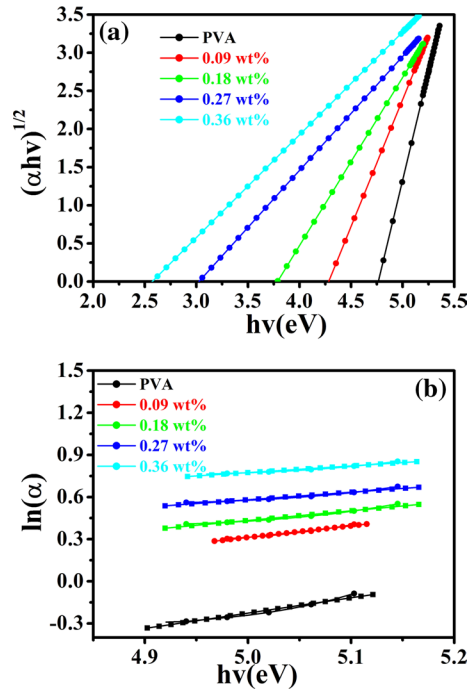


Table 1 Values of E_g and E_u corresponding to different amount of Ag_cAu_s NPs in PVA matrix

Specimen	E_g (eV)	E_u (eV)
PVA	4.70	0.91
0.09 wt% Ag_cAu_s PVA NC	4.28	1.21
0.18 wt% Ag_cAu_s PVA NC	3.78	1.47
0.27 wt% Ag_cAu_s PVA NC	3.0	1.88
0.36 wt% Ag_cAu_s PVA NC	2.57	2.12

host material, i.e. PVA, which increases the probability of low energy transitions, and these low energy transitions are responsible for the behaviour exhibited by E_g (decreases with increasing concentration of Ag_cAu_s NPs) and E_u (increases with increasing concentration of Ag_cAu_s NPs).

Behaviour of reflectance and refractive index ‘ n ’ for PVA and Ag_cAu_s PVA NC films shown in Fig. 10a and b, respectively. Figure 10a depicts that reflectance increases with incorporation of Ag_cAu_s NPs in PVA matrix. Moreover, a sudden dip is observed at a wavelength near to SPR peak for all Ag_cAu_s PVA NC. Reflectance increases considerably from 1.40% for PVA to 1.57% for 0.09 wt% of Ag_cAu_s NPs in PVA NC further to 1.69% for 0.18 wt%, 2.6% for 0.27 wt% and finally to 3.30% for 0.36 wt% of Ag_cAu_s NPs in PVA NC at 518 nm.

The refractive index ‘ n ’ is an essential parameter while deciding the utility of a material in optical devices such as modulators, switches, and filters [30]. Figure 10b

displays the variation of ‘ n ’ with ‘ λ ’ for PVA and Ag_cAu_s PVA NC, and it displays same behaviour as that of reflectance (Fig. 10a). Refractive index ‘ n ’ has been computed from the relation [41]:

$$n = \frac{1+R}{1-R} + \sqrt{\left(\frac{4R}{(1-R)^2}\right) - k^2} \quad (9)$$

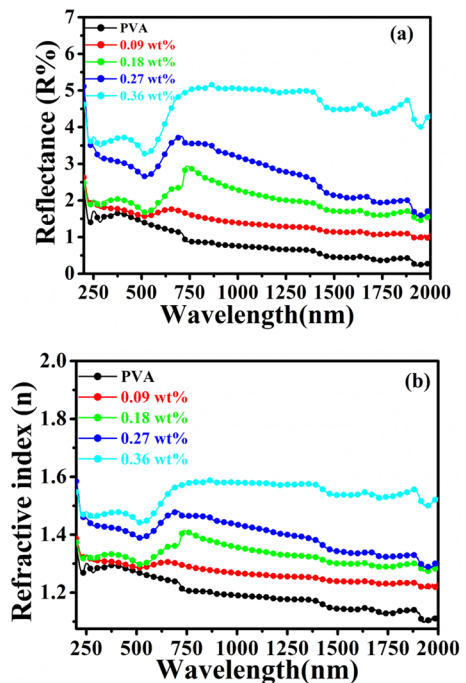
where R and k represent reflectance and extinction coefficient. k is determined from α and λ by:

$$k = \frac{\alpha\lambda}{4\pi} \quad (10)$$

Figure 10b demonstrates that ‘ n ’ increases from 1.26 for PVA to 1.28 for 0.09 wt% Ag_cAu_s PVA NC, to 1.30 for 0.18 wt%, to 1.38 for 0.27 wt% and finally to 1.40 for 0.36 wt% of Ag_cAu_s PVA NC at a wavelength of 518 nm. Addition of Ag_cAu_s NPs in PVA matrix increases the density of PVA films as high value of ‘ n ’ is a sign of high density of the films, which intern reduces the inter-atomic spacing [42]. Bulla et al. [28] and Mahmoud et al. [30] also observed similar results for Ag NPs embedded in PVA. They observed that ‘ n ’ of pure PVA is lower than that of Ag-PVA NC films.

‘ n ’ of a material depends on the wavelength of impinging electromagnetic radiation. If ‘ n ’ increases with increasing wavelength, then it is called anomalous dispersion;

Fig. 10 a Reflectance and b ‘ n ’ of PVA and Ag_cAu_s PVA NC films



if it decreases with increasing wavelength then it is called normal dispersion [40]. To analyse the ‘*n*’ in normal dispersion region, the single oscillator model developed by Wemple and Di-Domenico has been utilized [43]:

$$n^2 - 1 = \frac{E_0 E_d}{[E_0^2 - (hv)^2]} \tag{11}$$

Substituting $hv = 0$ in Eq. (11),

$$n_0 = \sqrt{1 + \frac{E_d}{E_0}} \tag{12}$$

where E_d represents dispersion energy, E_0 is the average excitation energy, n_0 (static refractive index) is the refractive index at $hv = 0$, ν represents frequency, and h is the Plank’s constant. Values of E_0 and E_d has been evaluated from the plot of $(n^2 - 1)^{-1}$ versus $(hv)^2$ as shown in Fig. 11. The intercept gives E_0/E_d and slope gives $(E_d E_0)^{-1}$. The values of E_0 , E_d , and n_0 for Ag_cAu_s PVA NC increases with increasing quantity of Ag_cAu_s NPs in PVA and are presented in Table 2. This increase in the value of E_0 , E_d , and n_0 for PVA with varying quantity of Ag_cAu_s NPs in PVA can be credited to the localized electronic states created within the HOMO–LUMO gap.

Further, E_0 , E_d , and n_0 have been used to evaluate linear optical susceptibility $\chi^{(1)}$ and various non-linear optical parameters such as third-order nonlinear optical susceptibility ($\chi^{(3)}$) and nonlinear refractive index (n_2), using following relations [43, 44]:

$$\chi^{(1)} = \frac{E_d}{4\pi E_0} \tag{13}$$

$$\chi^{(3)} = 6.82 \times 10^{-15} \left(\frac{E_d}{E_0}\right)^4 \tag{14}$$

$$n_2 = \frac{12\pi\chi^{(3)}}{n_0} \tag{15}$$

Fig. 11 Variation of $(n^2 - 1)^{-1}$ with $(hv)^2$ for PVA and Ag_cAu_s PVA NC

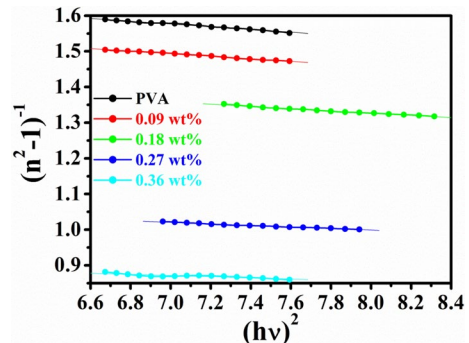


Table 2 Values of dispersion coefficients corresponding to different Ag_cAu_s NPs concentration in PVA matrix

Sample	E_0 (eV)	E_d (eV)	n_0	$\chi^{(1)}$	$\chi^{(3)}$, e.s.u	n_2 , e.s.u
PVA	6.92	3.75	1.24	0.0431	5.88×10^{-16}	1.78×10^{-14}
0.09 wt% Ag _c Au _s PVA NC	6.97	3.99	1.25	0.0455	6.96×10^{-16}	2.09×10^{-14}
0.18 wt% Ag _c Au _s PVA NC	7.09	4.49	1.27	0.0504	1.09×10^{-15}	3.23×10^{-14}
0.27 wt% Ag _c Au _s PVA NC	7.34	6.26	1.36	0.0679	3.60×10^{-15}	9.98×10^{-14}
0.36 wt% Ag _c Au _s PVA NC	7.74	7.85	1.41	0.0807	7.21×10^{-15}	19.14×10^{-14}

The values of $\chi^{(1)}$, $\chi^{(3)}$ and n_2 for Ag_cAu_s PVA NC increases with the increasing quantity of Ag_cAu_s NPs embedded in PVA and are presented in Table 2. The increase in the $\chi^{(3)}$ is attributed to a localized electric field arising due to core–shell structure of Ag and Au under off-surface-plasmon resonance conditions which increases with increasing content of Ag_cAu_s NPs in PVA [45]. As a consequence, the nonlinear optical parameters $\chi^{(1)}$, $\chi^{(3)}$ and n_2 increases. Soliman et al. [43] also observed similar results for Ni NPs in PVA. They observed that values of $\chi^{(1)}$, $\chi^{(3)}$, and n_2 increase with increasing content of Ni NPs in PVA and have attributed this increase to increasing volume fraction of Ni NPs. Materials with enhanced third-order optical nonlinearity have potential applications in nonlinear optical devices [4].

The optical conductivity (σ) represents the motion of charge carriers under the impact of high-frequency electromagnetic radiation and depends on speed of light (c), α and n by the following relation [40]:

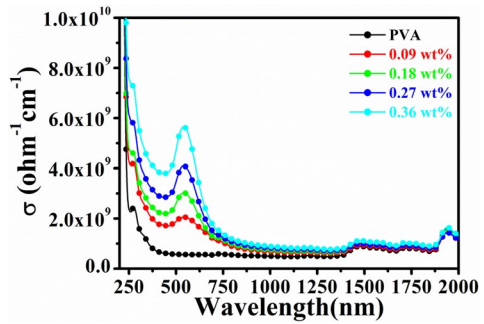
$$\sigma = \frac{\alpha n c}{4\pi} \quad (16)$$

Figure 12 illustrates the variation of optical conductivity of PVA and Ag_cAu_s PVA NC with wavelength. It can be seen that the optical conductivity increases with increasing amount of Ag_cAu_s NPs in PVA. This increase in optical conductivity is attributed to the greater probability of low energy transitions due to the creation of levels within the HOMO–LUMO gap of PVA.

I–V measurements

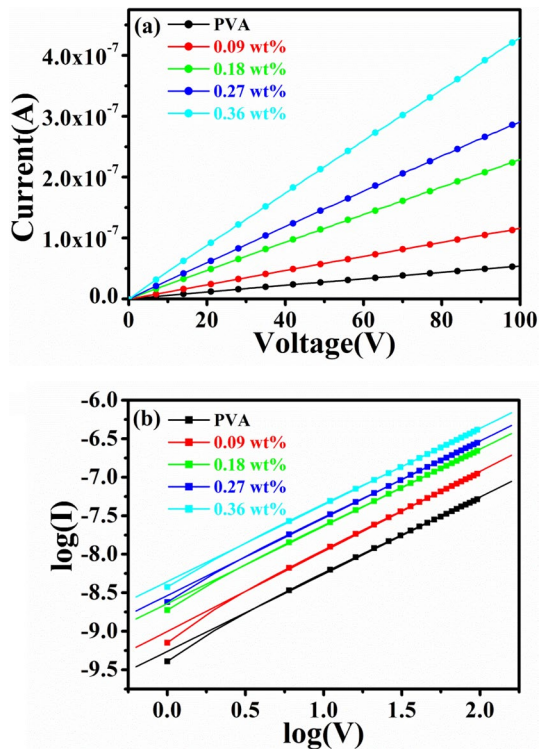
I–V characteristics of PVA and Ag_cAu_s PVA NC are linear as shown in Fig. 13a. Increase in current (I) at low voltage is slow, whereas it increases gradually at high voltage on incorporation of Ag_cAu_s NPs in the PVA matrix. Linear nature of I–V plots for PVA and Ag_cAu_s PVA NC indicates that conduction mechanism active in NC is ohmic. Plot of I–V characteristics in the form of $\log(I)$ versus $\log(V)$ is shown in Fig. 13b. In general, if the values of the slope (p) is 1, then the dominant conduction mechanism is ohmic, while the value of p is greater than 1 and less than equal to 1, then the leading conduction mechanism is either Schottky or Poole–Frenkel [46]. In the present study, slope of PVA and Ag_cAu_s PVA NC comes out to be nearly equal to $p = 1$ which indicates that the prevailing

Fig. 12 Optical conductivity (σ) with wavelength for PVA and Ag_cAu_s PVA NC



mechanism is ohmic. It is well-known that Au and Ag are good conductor, hence, it is expected that addition of Ag_cAu_s NPs in PVA matrix will improve its conductivity. Moreover, low energy transition occurring due to the creation of localized electronic states in the HOMO–LUMO region of PVA on addition of Ag_cAu_s NPs might be responsible for increased conductivity [47].

Fig. 13 a Variation of current (I) with voltage (V). **b** Plot of $\log(I)$ versus $\log(V)$ for PVA and Ag_cAu_s PVA NC



Conclusions

Ag_cAu_s NPs synthesized successfully via chemical reduction method have been used for fabrication of PVA-based NC films having different amounts of $C^{\text{Ag}}S^{\text{Au}}$ NPs by solution casting approach. Formation of peanut-shaped Ag_cAu_s NPs have been ascertained by using HRTEM and FESEM microscopy. SAED pattern and XRD analysis approves the crystalline nature of Ag_cAu_s NPs in PVA. The decrease in E_g and increase in E_u of PVA, with increasing quantity of Ag_cAu_s NPs, is due to the localized levels created in HOMO–LUMO region of PVA. Increase in the refractive index, optical conductivity, $\chi^{(1)}$, $\chi^{(3)}$, and n_2 for Ag_cAu_s PVA NC with the increasing quantity of Ag_cAu_s NPs in PVA are also among the major results of this report. The mechanism responsible for increased conductivity of PVA with increasing quantity of Ag_cAu_s NPs is ohmic.

Acknowledgements Authors are thankful to AIIMS, New Delhi for HRTEM and IIT Roorkee for FESEM measurements. R K acknowledges Council of Scientific & Industrial Research (CSIR), New Delhi, India, for Senior Research Fellowship.

Funding Funding was provided by Council of Scientific and Industrial Research, India (Grant No. 09/105/(0240)/2016-EMR-I).

Declarations

Conflict of interest The authors declare that they have no conflict of interest.

References

1. Han H, Fang Y, Li Z, Xu H (2008) Tunable surface plasma resonance frequency in Ag core/Au shell nanoparticles system prepared by laser ablation. *Appl Phys Lett* 92:023116. <https://doi.org/10.1063/1.2829588>
2. Nishi H, Hiroya S, Tatsuma T (2015) Potential-scanning localized surface plasmon resonance sensor. *ACS Nano* 9:6214–6221. <https://doi.org/10.1021/acsnano.5b01577>
3. Haes AJ, Zou S, Schatz GC, Van Duyne RP (2004) Nanoscale optical biosensor: short range distance dependence of the localized surface plasmon resonance of noble metal nanoparticles. *J Phys Chem B* 108:6961–6968. <https://doi.org/10.1021/jp036261n>
4. Ferreira E, Kharisov B, Vázquez A et al (2020) Tuning the nonlinear optical properties of Au@Ag bimetallic nanoparticles. *J Mol Liq* 298:112057. <https://doi.org/10.1016/j.molliq.2019.112057>
5. Sunaryono S, Rachmawati A, Yogihati CI et al (2021) The effect of Ag nanoparticles in Ag/polyvinyl alcohol nanofiber composites. *Polym Bull*. <https://doi.org/10.1007/s00289-020-03528-2>
6. Loiseau A, Zhang L, Hu D et al (2019) Core-shell gold/silver nanoparticles for localized surface plasmon resonance-based naked-eye toxin biosensing. *ACS Appl Mater Interfaces* 11:46462–46471. <https://doi.org/10.1021/acsmi.9b14980>
7. Yang L, Yan W, Wang H et al (2017) Shell thickness-dependent antibacterial activity and biocompatibility of gold@silver core-shell nanoparticles. *RSC Adv* 7:11355–11361. <https://doi.org/10.1039/C7RA00485K>
8. Yang J, Lee JY, Too H-P (2005) Core-shell Ag–Au nanoparticles from replacement reaction in organic medium. *J Phys Chem B* 109:19208–19212. <https://doi.org/10.1021/jp052242x>
9. Mott D, Lee J, Thuy NTB et al (2011) A study on the plasmonic properties of silver core gold shell nanoparticles: optical assessment of the particle structure. *Jpn J Appl Phys* 50:065004. <https://doi.org/10.1143/JJAP.50.065004>

10. Singh P, Thuy NTB, Aoki Y et al (2011) Intensification of surface enhanced Raman scattering of thiol-containing molecules using Ag@Au core@shell nanoparticles. *J Appl Phys* 109:094301. <https://doi.org/10.1063/1.3579445>
11. Vinod M, Gopchandran KG (2015) Ag@Au core-shell nanoparticles synthesized by pulsed laser ablation in water: effect of plasmon coupling and their SERS performance. *Spectrochim Acta Part A Mol Biomol Spectrosc* 149:913–919. <https://doi.org/10.1016/j.saa.2015.05.004>
12. Miao X, Zou S, Zhang H, Ling L (2014) Highly sensitive carcinoembryonic antigen detection using Ag@Au core-shell nanoparticles and dynamic light scattering. *Sens Actuators B Chem* 191:396–400. <https://doi.org/10.1016/j.snb.2013.10.016>
13. Cao JR, Mirkin CA (2001) DNA-modified core-shell Ag/Au nanoparticles. *J Am Chem Soc* 123:7961–7962. <https://doi.org/10.1021/ja011342n>
14. Hamidi-Asl E, Dardenne F, Pilehvar S et al (2016) Unique properties of core shell Ag@Au nanoparticles for the aptasensing of bacterial cells. *Chemosensors* 4:16. <https://doi.org/10.3390/chemosensors4030016>
15. Lee H, Hong S, Lee J et al (2016) Highly stretchable and transparent supercapacitor by Ag–Au core-shell nanowire network with high electrochemical stability. *ACS Appl Mater Interfaces* 8:15449–15458. <https://doi.org/10.1021/acsami.6b04364>
16. Zhao Y, Yang Y, Luo Y et al (2015) Double detection of mycotoxins based on SERS labels embedded Ag@Au core-shell nanoparticles. *ACS Appl Mater Interfaces* 7:21780–21786. <https://doi.org/10.1021/acsami.5b07804>
17. Ezhil Vilian AT, Shahzad A, Chung J et al (2017) Square voltammetric sensing of mercury at very low working potential by using oligomer-functionalized Ag@Au core-shell nanoparticles. *Microchim Acta* 184:3547–3556. <https://doi.org/10.1007/s00604-017-2372-3>
18. Lai W, Zhou J, Jia Z et al (2015) Ag@Au hexagonal nanorings: synthesis, mechanistic analysis and structure-dependent optical characteristics. *J Mater Chem C* 3:9726–9733. <https://doi.org/10.1039/C5TC02017D>
19. Khlebtsov BN, Liu Z, Ye J, Khlebtsov NG (2015) Au@Ag core/shell cuboids and dumbbells: optical properties and SERS response. *J Quant Spectrosc Radiat Transf* 167:64–75. <https://doi.org/10.1016/j.jqsrt.2015.07.024>
20. Rai A, Chaudhary M, Ahmad A et al (2007) Synthesis of triangular Au core–Ag shell nanoparticles. *Mater Res Bull* 42:1212–1220. <https://doi.org/10.1016/j.materresbull.2006.10.019>
21. Jun Yin H, Yang Chen Z, Mei Zhao Y et al (2015) Ag@Au core-shell dendrites: a stable, reusable and sensitive surface enhanced Raman scattering substrate. *Sci Rep* 5:14502. <https://doi.org/10.1038/srep14502>
22. Li D, Zhang X, Zhu J et al (2020) Shuttle-like core-shell gold nanorod@Ag–Au nanostructures: shape control and electrocatalytic activity for formaldehyde oxidation. *Appl Surf Sci* 528:146935. <https://doi.org/10.1016/j.apsusc.2020.146935>
23. Sanedrin RG, Georganopoulou DG, Park S, Mirkin CA (2005) Seed-mediated growth of bimetallic prisms. *Adv Mater* 17:1027–1031. <https://doi.org/10.1002/adma.200402022>
24. Deb S, Sarkar D (2021) Polyvinyl alcohol–silver fractal structured nanodendrites: photochemical synthesis. *Polym Bull* 78:81–91. <https://doi.org/10.1007/s00289-019-03097-z>
25. Matar GH, Andac M (2020) Antibacterial efficiency of silver nanoparticles-loaded locust bean gum/polyvinyl alcohol hydrogels. *Polym Bull*. <https://doi.org/10.1007/s00289-020-03418-7>
26. Saini I, Rozra J, Chandak N et al (2013) Tailoring of electrical, optical and structural properties of PVA by addition of Ag nanoparticles. *Mater Chem Phys* 139:802–810. <https://doi.org/10.1016/j.matchemphys.2013.02.035>
27. Tripathi J, Keller JM, Das K et al (2012) Influence of Rhodamine (B) doping on vibrational, morphological and absorption properties of poly(vinyl) alcohol. *J Phys Chem Solids* 73:1026–1033. <https://doi.org/10.1016/j.jpcs.2012.03.011>
28. Bulla SS, Bhajantri RF, Chavan C (2021) Optical and structural properties of biosynthesized silver nanoparticle encapsulated PVA (Ag–PVA) films. *J Inorg Organomet Polym Mater* 31:2368–2380. <https://doi.org/10.1007/s10904-021-01909-2>
29. El-Shamy AG, Attia W, Abd El-Kader KM (2014) The optical and mechanical properties of PVA–Ag nanocomposite films. *J Alloys Compd* 590:309–312. <https://doi.org/10.1016/j.jallcom.2013.11.203>
30. Mahmoud KH (2015) Synthesis, characterization, optical and antimicrobial studies of polyvinyl alcohol–silver nanocomposites. *Spectrochim Acta Part A Mol Biomol Spectrosc* 138:434–440. <https://doi.org/10.1016/j.saa.2014.11.074>

31. Som T, Karmakar B (2009) Core–shell Au–Ag nanoparticles in dielectric nanocomposites with plasmon-enhanced fluorescence: a new paradigm in antimony glasses. *Nano Res* 2:607–616. <https://doi.org/10.1007/s12274-009-9061-4>
32. Mallick S, Sanpui P, Ghosh SS et al (2015) Synthesis, characterization and enhanced bactericidal action of a chitosan supported core–shell copper–silver nanoparticle composite. *RSC Adv* 5:12268–12276. <https://doi.org/10.1039/C4RA12770F>
33. Cullity BD (1978) *Elements of X-ray diffraction*. Addison-Wesley Publishing Company Inc., San Francisco
34. Birkholz M, Fewster PF, Genzel C (2006) Thin film analysis by X-ray diffraction
35. Rajender G, Giri PK (2016) Strain induced phase formation, microstructural evolution and band-gap narrowing in strained TiO₂ nanocrystals grown by ball milling. *J Alloys Compd* 676:591–600. <https://doi.org/10.1016/j.jallcom.2016.03.154>
36. Nath D, Singh F, Das R (2020) X-ray diffraction analysis by Williamson–Hall, Halder–Wagner and size-strain plot methods of CdSe nanoparticles—a comparative study. *Mater Chem Phys* 239:122021. <https://doi.org/10.1016/j.matchemphys.2019.122021>
37. Gamler JTL, Leonardi A, Sang X et al (2020) Effect of lattice mismatch and shell thickness on strain in core@shell nanocrystals. *Nanoscale Adv* 2:1105–1114. <https://doi.org/10.1039/d0na00061b>
38. Murugavelu M, Karthikeyan B (2017) Synthesis, characterization of Ag–Au core–shell bimetal nanoparticles and its application for electrocatalytic oxidation/sensing of l-methionine. *Mater Sci Eng C* 70:656–664. <https://doi.org/10.1016/j.msec.2016.09.046>
39. Mott NF, Davis EA (1971) *Electronic processes in non-crystalline materials*. Oxford University Press, New York
40. Sonal SA, Aggarwal S (2018) Silver glass nanocomposites synthesised by 200 keV Ar⁺ ions at oblique incidence for potential applications as filters in mid infrared region. *Opt Mater (Amst)* 84:807–812. <https://doi.org/10.1016/j.optmat.2018.08.022>
41. Ahmad AA, Alsaad AM, Al-Bataineh QM, Al-Naafa MA (2018) Optical and structural investigations of dip-synthesized boron-doped ZnO-seeded platforms for ZnO nanostructures. *Appl Phys A* 124:458. <https://doi.org/10.1007/s00339-018-1875-z>
42. Abdelaziz M (2011) Cerium (III) doping effects on optical and thermal properties of PVA films. *Phys B Condens Matter* 406:1300–1307. <https://doi.org/10.1016/j.physb.2011.01.021>
43. Soliman TS, Vshivkov SA, Elkalashy SI (2020) Structural, linear and nonlinear optical properties of Ni nanoparticles—polyvinyl alcohol nanocomposite films for optoelectronic applications. *Opt Mater (Amst)* 107:110037. <https://doi.org/10.1016/j.optmat.2020.110037>
44. Flytzanis C, Hache F, Klein MC et al (1991) V nonlinear optics in composite materials: 1. Semiconductor and metal crystallites in dielectrics. *Prog Opt* 29:321–411
45. Yang Y, Nogami M, Shi J et al (2005) Enhancement of third-order optical nonlinearities in 3-dimensional films of dielectric shell capped Au composite nanoparticles. *J Phys Chem B* 109:4865–4871. <https://doi.org/10.1021/jp045854a>
46. Anjaneyulu P, Sangeeth CSS, Menon R (2010) Space-charge limited conduction in doped polypyrrole devices. *J Appl Phys* 107:093716. <https://doi.org/10.1063/1.3373393>
47. Blythe T, Bloor D (2005) *Electrical properties of polymers*. Cambridge University Press, Cambridge

Publisher's Note Springer Nature remains neutral with regard to jurisdictional claims in published maps and institutional affiliations.

Springer Nature or its licensor holds exclusive rights to this article under a publishing agreement with the author(s) or other rightsholder(s); author self-archiving of the accepted manuscript version of this article is solely governed by the terms of such publishing agreement and applicable law.